A Global Optimal Solution With Higher Order Continuity for the Estimation of Surface Velocity From Infrared Images

Wei Chen

***Abstract*—A global optimal solution (GOS) provides surface velocities from Advanced Very High Resolution Radiometer (AVHRR) remote image sequences using bilinear interpolation algorithms. Although an accurate velocity field can be estimated by GOS from a sequence of infrared images, the field has only first-order continuity. Because an actual coastal ocean has a complex irregular coastland and some ocean studies need vorticity and divergence analysis, which must be extracted from the velocity field, the development of generic GOS algorithms with higher order continuity and smoothed cutouts around these edges is very important. This paper addresses the issues of higher order continuity and smoothed cutouts around coastland edges for using GOS to estimate surface velocities. GOS bilinear polynomials, previously applied to square tiles with first-order continuity, are replaced by surface B-spline functions. The new GOS algorithms can be applied to AVHRR images containing complicated coastal land boundaries, even clouds, to yield smooth velocity fields next to land and higher order continuity velocity fields. The velocity fields obtained through the applications of the first- and higher order GOS techniques to a sequence of two National Oceanic Atmospheric Administration AVHRR images, which were taken from the New York Bight fields, are compared with those measured with the CODAR array. The retrieved velocity fields are used directly to calculate the surface divergence and vorticity. It is found that the angular and magnitude errors of the velocity by the first- and third-order GOSs are quite close for both numerical model data and AVHRR image sequences, and the velocity field estimated by the third-order GOS is globally smoothed.**

***Index Terms*—Global optimal solution (GOS), infrared images, inverse model, motion estimation, velocity estimation.**

I. Introduction

ACCURATELY estimating ocean currents at geophysical scales is a formidable task, requiring high-fidelity spatial and temporal observations. Satellite-based methods have the potential for providing this information, and methods for estimating surface currents from the advection of features observed in sequential satellite images of large-scale oceanic flows have been sought for more than 20 years. A variety of methods are available for surface current estimation from sequential imagery. At present, we are concerned with the inversion of a heat equation to obtain the velocity field at the ocean surface.

Since the introduction of the seminal works by Kelly [1] and Kelly and Strub [2], the inverse technique has been employed and developed in several papers. For example, it has been employed to infer the properties of the ocean surface mixed layer. Ostrovskii and Piterbarg [3], [4] invert an advection–diffusion equation for the upper ocean mixed layer in different areas of the Pacific Ocean for velocity, as well as vertical mixed-layer entrainment velocity and horizontal diffusivity. Using model-generated data, Vigan *et al.* [5], [6] demonstrate the utility of the method for the Brazil–Malvinas confluence region, while Zavialov *et al.* [7] have performed a similar calculation for the same region using sea-surface temperature (SST) data mapped from *in situ* measurements. Recently, there have been some different conceptual approaches in estimating geophysical flow [8]. Marcello *et al.* [9] performed evaluation and detailed studies of popular motion estimation techniques in the computer-vision field applying to applications of remote sensing.

The global optimal solution (GOS) of Chen *et al.* [10] provides surface velocities from Advanced Very High Resolution Radiometer (AVHRR) remote image sequences. They find that the verifiable accuracy obtained is much better than the previously reported for several reasons. First, they do not impose the constraints used in the inverse method of Chen *et al.* [10]. Second, they do not smooth the data but remove only broad-area trends. All of the finer scale surface isotherm structures are thus retained, and these structures provide unambiguous features for tracking and inversion. To solve velocities with the GOS method, an unmasked domain of an image sequence has been divided into many smaller subdomains or "tiles." If a tile contains any land or cloud contamination, that tile is discarded, so that the resulting near-shore coverage is jagged. Since the velocity was expanded by first-order continuity surface polynomials, it is difficult to calculate vorticity and divergence based on the estimated velocity field by the first-order GOS without preprocessing.

This paper addresses the issues of higher order continuity and smoothed cutouts around coastland edges for using GOS to estimate surface velocities. GOS bilinear polynomials, previously applied to square tiles with first-order continuity, are replaced by surface B-spline functions [13]. The degree of the continuity is determined by the user; thus, the GOS methods can handle complicated unmasked areas, which contain

Manuscript received May 14, 2009; revised September 23, 2009. First published January 12, 2010; current version published March 24, 2010. This work was supported by the Office of Naval Research through Project WU-8743-07 at the Naval Research Laboratory.

The author is with the Remote Sensing Division, Naval Research Laboratory, Washington, DC 20375 USA (e-mail: wei.chen@nrl.navy.mil).

Color versions of one or more of the figures in this paper are available online at http://ieeexplore.ieee.org.

Digital Object Identifier 10.1109/TGRS.2009.2037316

shorelines or clouds. These pixel subsets are melded into a single high-order continuous velocity field for the entire image scene. The velocity is thus globally valid and is chosen as an optimal solution to the heat equation. The vertical entrainment and diffusive effects are grouped into a single function of the horizontal spatial variables and solved for this field and velocity simultaneously to yield a GOS. In addition, the number of control points in the B-spline functions on the whole unmasked scene is chosen so that the problem is a determinate one without additional constraints on the velocity field. The fidelity of the solutions is evaluated by comparing it with the output of a 3-D nonhydrostatic numerical ocean model.

This paper is organized as follows. In Section II, the model and associated algorithms are described. Section III deals with the validation of the technique by deriving velocity from synthetic tracer motion within a numerical ocean model and detailed statistical comparisons among the current fields obtained by the previous first-order GOS and this high-order GOS. The utility of the results is demonstrated in Section IV, where the GOS technique is applied to two AVHRR image pairs from the North Atlantic Ocean. Conclusions are drawn in Section V.

II. Tracer Conservation Equation

A. Tracer Conservation Equation

The heat flow of an image sequence is a set of vector fields, relating each image to the next. Each vector field represents the apparent displacement of each pixel from image to image. The evolution of temperature field in a 2-D surface of ocean is governed by the heat equation [1], [10]

$$T_t + uT_x + \nu T_y = s \tag{1}$$

where u and ν are the heat flow components in the x- and y-directions for a displacement and T_x, T_y, and T_t are the partial derivatives of the temperature $T = T(x, y, t)$ with regard to the x- and y-coordinates and time t. The heat flow vector is defined by $\mathbf{v} = (u(x, y, t), v(x, y, t))$. The variable $s = s(x, y, t)$ is a source term containing the effects of air–sea interaction and turbulent processes within the mixed layer (see, e.g., [10]). Here, we have three unknowns in only one equation; thus, the problem is ill posed, and extra constraints must be imposed in order to arrive at a solution.

B. Expansions of Velocity Field and Source

The temporal and spatial derivatives of the temperature flow fields in (1) can be calculated from the temperature flow fields on the image sequence. The problem is underdetermined, however, because three unknowns u, ν, and s must be derived from a single heat equation (1) at each of these pixel points.

This new approach is to expand the velocity fields and source terms $\{u(x, y), \nu(x, y), s(x, y)\}$ as 2-D B-spline functions [13] on the whole image scene

$$\{u(x,y), \nu(x,y), s(x,y)\} = \sum_{p=0}^{Nc_x} \sum_{q=0}^{Nc_y} \{cpu_{pq}, cp\nu_{pq}, cps_{pq}\} N_{pn}(x) N_{qn}(y) \tag{2}$$

where $\{cpu_{ij}, cp\nu_{ij}, cps_{ij}\}$, n, $Nc_x + 1$, $Nc_y + 1$, $N_{pn}(x)$, and $N_{qn}(y)$ are the control points for each $\{u, \nu, s\}$, the order of B-splines, the number of control points on the x- and y-directions, and blending functions, respectively. The total number of control points, which is also the total number of unknown parameters for all components in (2) for all image pixels, is given by

$$N_{cp} = 3(Nc_x + 1)(Nc_y + 1). \tag{3}$$

Substituting (2) into (1), we found

$$T_t(x,y) = \sum_{p=0}^{Nc_x} \sum_{q=0}^{Nc_y} [cps_{pq} - cpu_{pq} T_x(x,y) - cp\nu_{pq} T_y(x,y)] N_{pn}(x) N_{qn}(y) \tag{4}$$

where p and q are the control point indices. To easily deal with the math problem and the next step discussion, we introduce a single index mapping function α by

$$\alpha = \alpha(k,p,q) = 1 + k + N_c\,(p + q(Nc_x + 1)) \quad \forall\ (p \in \{0, 1, \ldots, Nc_x\}, q \in \{0, 1, \ldots, Nc_y\}, k \in \{0, 1, \ldots, N_c\}) \tag{5}$$

where $N_c = 3$ or 2 (if we ignore the source term) and $\alpha \in \{1, 2, \ldots, N_{cp}\}$. Introducing a new parameter a_α with a single index α, we have

$$a_\alpha = \begin{cases} cpu_{pq}, & (k = 0, 0 \le p \le Nc_x, 0 \le q \le Nc_y) \\ cp\nu_{pq}, & (k = 1, 0 \le p \le Nc_x, 0 \le q \le Nc_y) \\ cps_{pq}, & (k = 2, 0 \le p \le Nc_x, 0 \le q \le Nc_y) \end{cases}$$

and a new extended blending function is also defined by

$$B_\alpha(x,y) = \begin{cases} -T_x(x,y) N_{pn}(x) N_{qn}(y), & (k = 0) \\ -T_y(x,y) N_{pn}(x) N_{qn}(y), & (k = 1) \\ N_{pn}(x) N_{qn}(y), & (k = 2). \end{cases}$$

Then, we can rewrite (4) in a more compact form that is suitable for incorporation into the formalism described in the next section as

$$T_t(x,y,t) = \sum_{\alpha=1}^{N_{cp}} a_\alpha(t) B_\alpha(x,y). \tag{6}$$

Now, we can solve the aforementioned system of equations to find the solution of the heat equations on the image sequence, if the total number of unknown parameters a_α is exactly equal to the total number of pixels. A flexible treatment of the problem is that which seeks a solution with adjustable parameters (the number of unknown parameters) to obtain an optimized solution.

C. GOS

A chi-squared function expresses the error in fitting a set of a_α to the data; it is defined by

$$\chi^2 = \sum_{i=1}^{N} \left(\frac{\Delta T_i}{\Delta t} - \sum_{\alpha=1}^{N_{cp}} a_\alpha B_{\alpha,i} \right)^2$$

where $N = N_x N_y$ is the total number of pixels and $B_{\alpha,i} = B_\alpha(x,y) \forall\, (i = x + (y-1)N_x)$.

A GOS can be obtained by minimizing χ^2 with respect to a_α. This minimization procedure is a linear regression problem, which results in the following linear system of equations for the matrix $\mathbf{a}(\equiv a_\alpha)$:

$$\mathbf{a} = \mathbf{L}^{-1}\mathbf{b} \tag{7}$$

where

$$L_{\alpha\beta} = \frac{1}{N}\sum_{i=1}^{N} B_{\alpha,i}B_{\beta,i} \qquad b_\alpha = \frac{1}{N}\sum_{i=1}^{N} B_{\alpha,i}\frac{\Delta T_i}{\Delta t}. \tag{8}$$

$\boldsymbol{L}$ is an $N_{cp} \times N_{cp}$ correlation matrix between $B_{\alpha,i}$ and $B_{\beta,i}$, and $\mathbf{b}$ is an N_{cp}-dimensional correlation vector between $B_{\alpha,i}$ and $\Delta T_i/\Delta t$. Since N_{cp} is dependent on the number of pixels for a particular image sequence, a selected number of control points N_{cp} will normally be on the order of hundreds to thousands. The heat equation thus becomes a global linear optimization problem, and velocity fields and source terms can be computed over the whole image by (2). We can adjust the order of B-spline function to control the order of continuity for the vector field and also the number of control points of the B-spline function to get from high to low resolutions of the structures for the velocity field.

D. Computing Algorithms

To solve the system of equations (7), we must calculate a correlation matrix $\boldsymbol{L}$ first. Using the index mapping function defined in (5), this correlation matrix is a band diagonal, and the width of the band depends on the Nc_x, Nc_y, and the order of B-spline function. If we consider the nonzero terms in the matrix $\boldsymbol{L}$ that is only related to the neighborhood points of the spatial mapping position of the index α, then a refining designed program for the calculation of the correlation (8) can greatly accelerate the computation speed. Let us define the neighborhood points of the spatial mapping position of the index α within an unmasked image region $\Omega = \Omega(\alpha)$; then, the correlation matrix $\boldsymbol{L}$ defined in (8) can be modified by

$$L_{\alpha\beta} = \frac{1}{N}\sum_{i\in\Omega} B_{\alpha,i}B_{\beta,i}. \tag{9}$$

Once matrix $\boldsymbol{L}$ is obtained, the positive definite band-diagonal matrix can be solved by a regular linear subroutine.

An example of a realistic AVHRR image with a masked region and selected control points is shown in Fig. 1. The solid red dots are used to indicate the positions of the control points, and the summation index i in (9) goes over all unmasked pixels (within the Ω region), as shown in Fig. 1.

III. Experimental Results and Analysis

The performance of GOS with first-order continuity test and applications has been demonstrated in the paper by Chen *et al.* [10]. To assess the ability of the present method to obtain surface velocities, we still use the solution of a numerical model as a benchmark and introduce a surface tracer field as an initial condition. The angular and magnitude measures of error are introduced in this paper, and the mean values of these errors are applied to evaluate the performance of the velocity estimations.

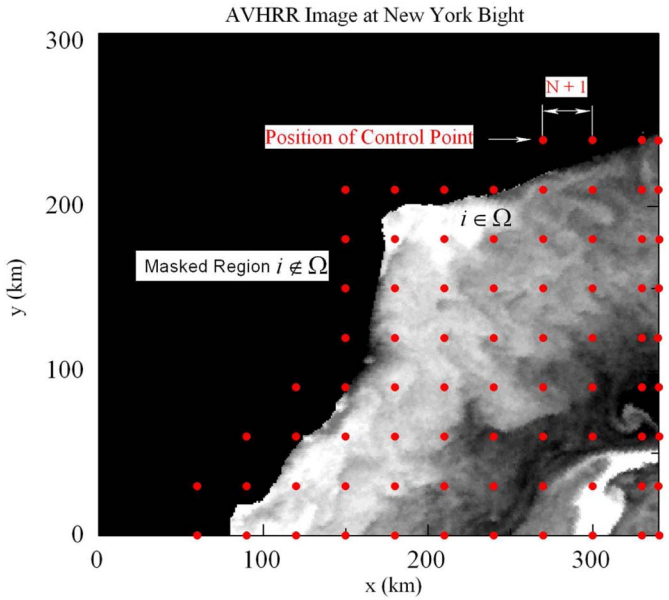

Fig. 1. Example of masked AVHRR image with the positions of control points labeled by solid red dots.

A. Numerical Model

A simulated flow field and its advection of SST are obtained by solving 3-D nonlinear fluid dynamical equations and the equation for the tracer (or temperature). For the purposes here, the temperature T is treated simply as a passive tracer with a weak diffusivity added for numerical stability (see [10]).

The inversion of the simulated SST for surface flow is performed using the nth-order GOS method for a range of control points. The number of pixels between two control points is defined by $N-1$. In terms of the number of control points, the smallest array size tested has the dimension of $N = 8$ points on each side (see Fig. 1), and the largest one has 20. In the calculations reported here, only the cubic B-spline function $(n = 4)$ in (3) is used. Therefore, the order of continuity of the velocity fields estimated by the GOS is equal to three. The benchmark velocity vectors given by the numerical model are shown in Fig. 2(a), and for comparison, vectors estimated by the third-order GOS with B-spline functions are shown in Fig. 2(b). The number of pixels between two control points used to obtain this GOS result is $N = 11$ grid points wide on each side. The false-color presentation of images in the background is the tracer field (or simulated SST) with scales ranging from 0 to 50 km in horizontal and vertical, which, by the time from 18 to 20 h, has been deformed by the currents and is significantly different from its original $\sin(2\pi x/L)\sin(2\pi y/L)$ square cell shape.

The two velocity vector fields in Fig. 2 are mutually similar, with each showing a distribution of eddies having diameters on

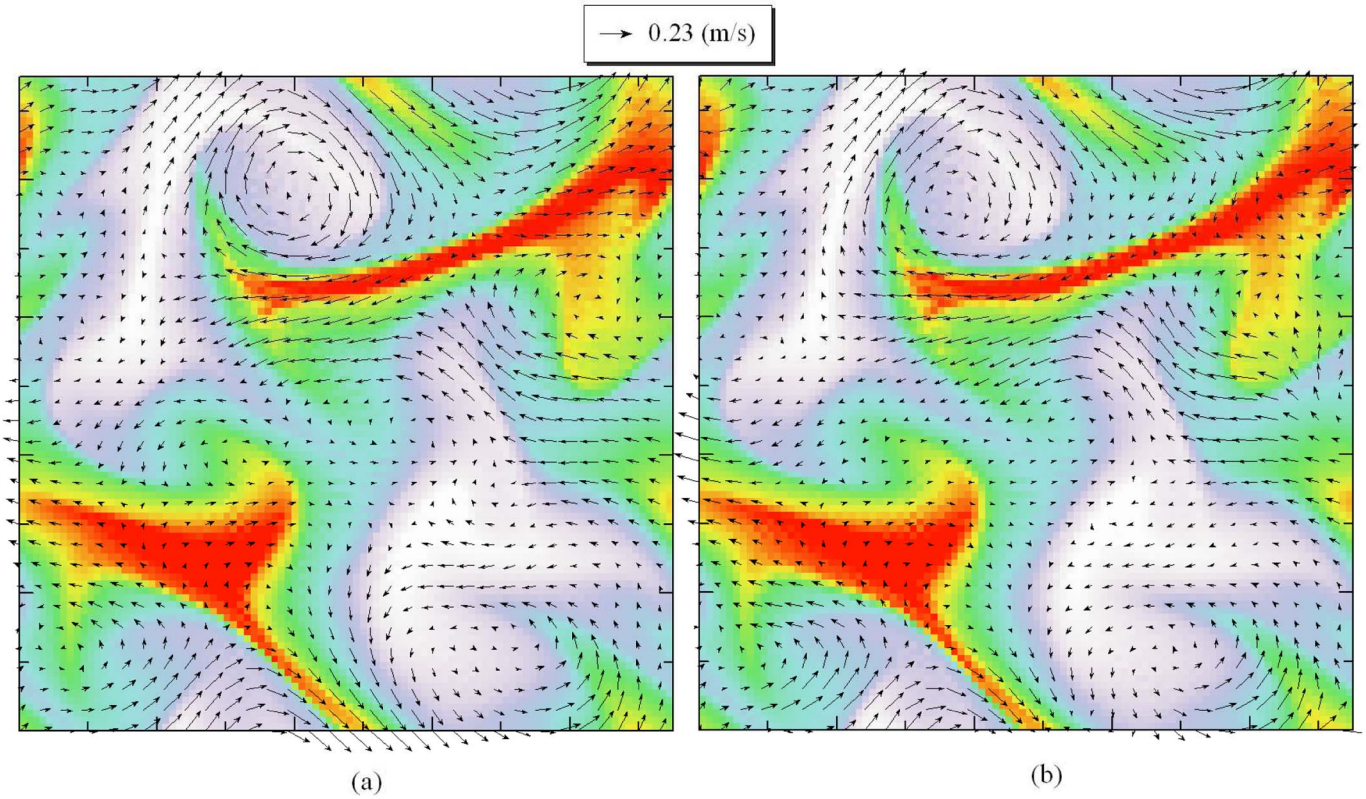

Fig. 2. Velocity fields: (a) and (b) Averages of the modeled velocity fields generated by the model at time $t_1 = 18$ h and $t_2 = 20$ h. (b) Estimated vector fields obtained from the third-order GOS between t_1 and t_2.

the order of 15 km and more gently curved tendril structures with larger radii of curvature. There are three prominent eddies in the modeled tracer field [Fig. 2(a)], with centers located at ∼(5 km, 5 km), (36 km, 5 km), and (21 km, 40 km). The third-order GOS results [Fig. 2(b)] capture these features qualitatively well and represent them as well-defined vortices. Two examples of this are the jets of fluid exiting the left edge of the box at $y \approx 25$ km and the one at the upper right-hand corner.

The velocity fields with two components u and ν generated by a numerical ocean model at time $t_1 = 18$ h and $t_2 = 20$ h and estimated by the first- and third-order GOSs are displayed as images, as shown in Fig. 3. The velocity field images (c) and (f) are estimated by the third-order GOS and demonstrate that the fields with higher order continuity are obviously comparable to the fields estimated by the first-order GOS.

B. Error Measurement

The angular and magnitude measures of error are used in this paper. Velocity may be written as $\mathbf{v} = (u, \nu, 0)$ (assuming that the component of velocity in z is $w = 0$), and then, the angular and magnitude errors between the correct velocity $\mathbf{v}_c$ and an estimate $\mathbf{v}_e$ are

$$\Delta\theta = \arccos\left(\frac{\mathbf{v}_c \cdot \mathbf{v}_e}{|\mathbf{v}_c||\mathbf{v}_e|}\right) = \arccos\left(\frac{u_e u_c + \nu_e \nu_c}{\sqrt{u_c^2 + \nu_c^2}\sqrt{u_e^2 + \nu_e^2}}\right) \tag{10}$$

$$\Delta V = \frac{|\mathbf{v}_c - \mathbf{v}_e|^2}{|\mathbf{v}_c||\mathbf{v}_e|} = \frac{(u_e - u_c)^2 + (\nu_e - \nu_c)^2}{\sqrt{u_c^2 + \nu_c^2}\sqrt{u_e^2 + \nu_e^2}} \tag{11}$$

where magnitude errors are a dimensionless quantity. The mean values of the angular and magnitude errors between the correct velocity $\mathbf{v}_c$ and an estimate $\mathbf{v}_e$ are used to evaluate the performance of the velocity estimations.

The aforementioned comparisons between Fig. 2(a) and (b) have been qualitative. The quantitative measures of how well the first- and third-order GOSs can reproduce the model flow are shown in Fig. 4, in which the mean values of the angular and magnitude errors versus N are shown.

Both curves of the angular and magnitude errors generated by the first- and third-order GOSs exhibit a local minimum in the vicinity of $N \approx 10$ and 11, and two competing phenomena, one at small N and another for large, are responsible for this. When N is small, the number of B-spline squares required to cover the image must be large (Fig. 1). Both curves of the angular and magnitude errors shown in Fig. 4 indicate that there are no significant differences between $N = 8$ and 15, in which range N is highly recommended.

The system is not strongly overdetermined because there are a few N points over which to fit to the B-spline velocity expression to each square. As N increases, however, the B-spline fits become less accurate (the number of control points decreases), and the angular and magnitude errors of the estimated velocities increase. The offsetting effect occurs for very large N. There, the number of control points used to tile the image decreases

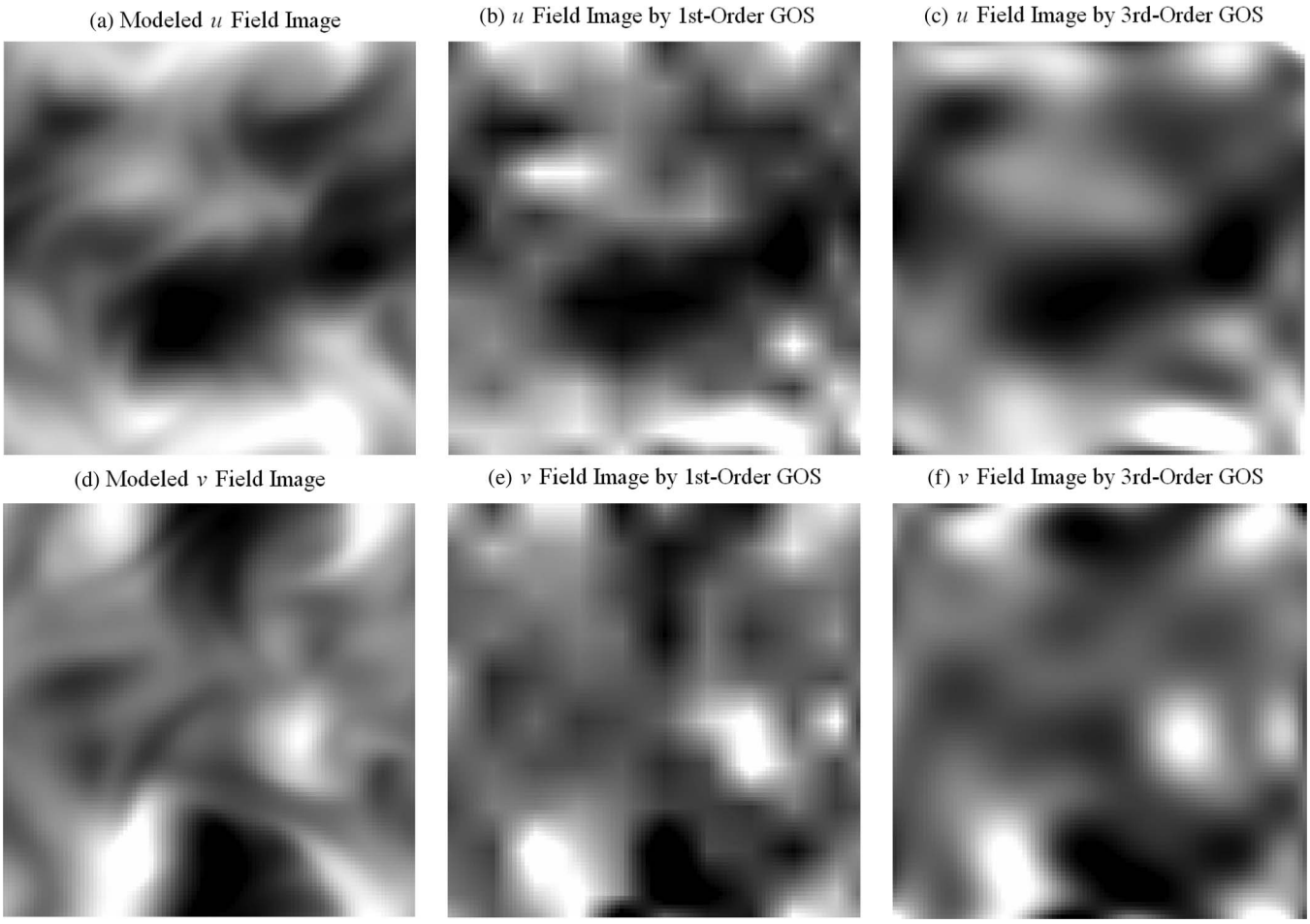

Fig. 3. Velocity field images with two components u and ν that have ranges from dark (-0.23 m/s) to light (0.23 m/s) regions approximately. (a) and (d) Averages of the modeled vector field images generated by the model at time $t_1 = 18$ h and $t_2 = 20$ h. (b), (c), (e), and (f) Estimated vector field images obtained from the first- and third-order GOSs between t_1 and t_2.

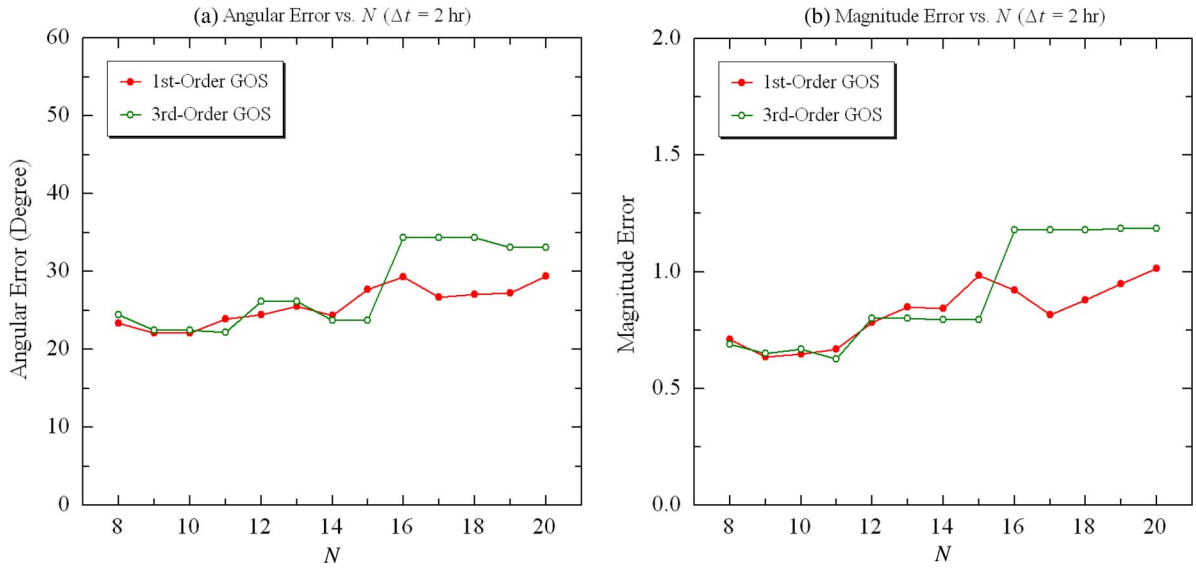

Fig. 4. Plots of error measurement generated by the first- and third-order GOSs with numerical model data at time $t_1 = 18$ h and $t_2 = 20$ h. (a) Mean values of angular error defined by (10) versus N (the number of pixels between two control points). (b) Mean values of magnitude error defined by (11) versus N.

markedly. Consequently, a potentially complex tracer distribution must be described with far fewer B-spline expressions, and the accuracy must decrease. Larger values of N thus reduce our ability to capture small-scale variability in the velocity field, which accounts for the increasing error for large N. The net effect of these two competing phenomena is the local minimum

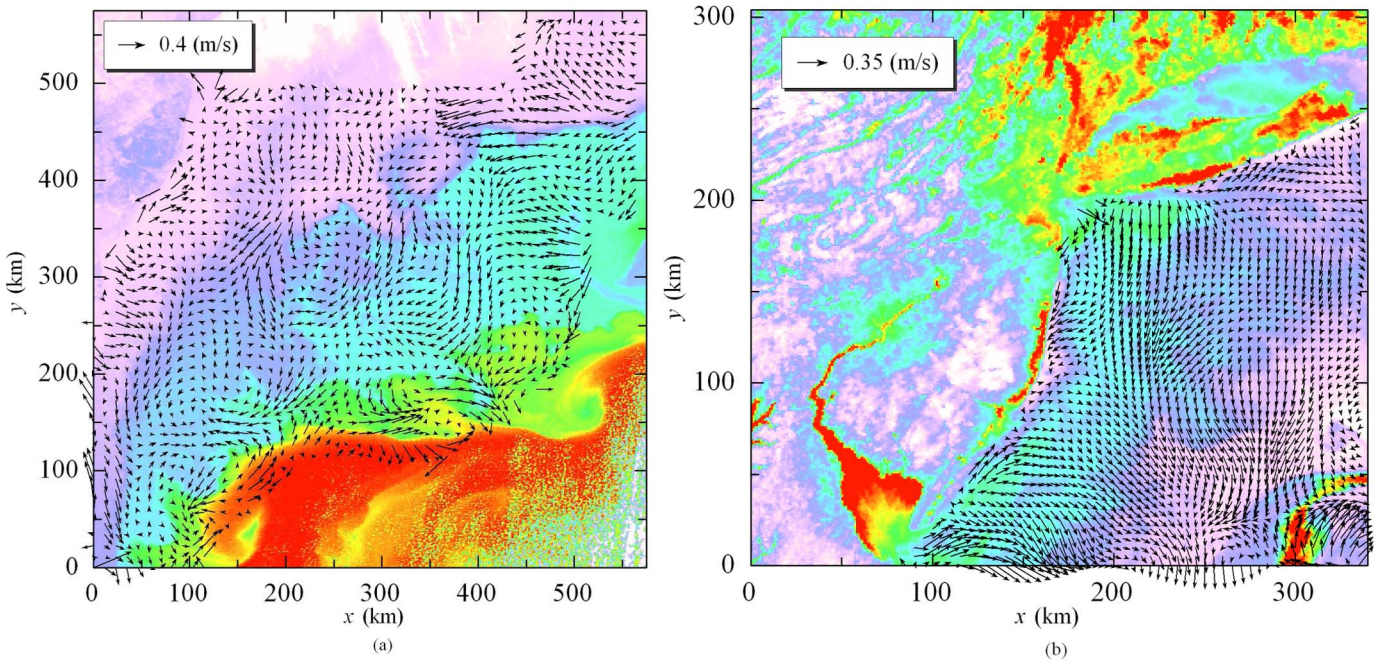

Fig. 5. Vector field derived from the AVHRR image (false-color representations) sequences within an unmasked region. (a) February 28, 2004 at 19:02–22:32 UT. (b) May 26, 2007 at 7:21–10:46 UT. Vectors are plotted at every (a) tenth pixel and (b) fifth pixel, and the image shown is the second of each pair.

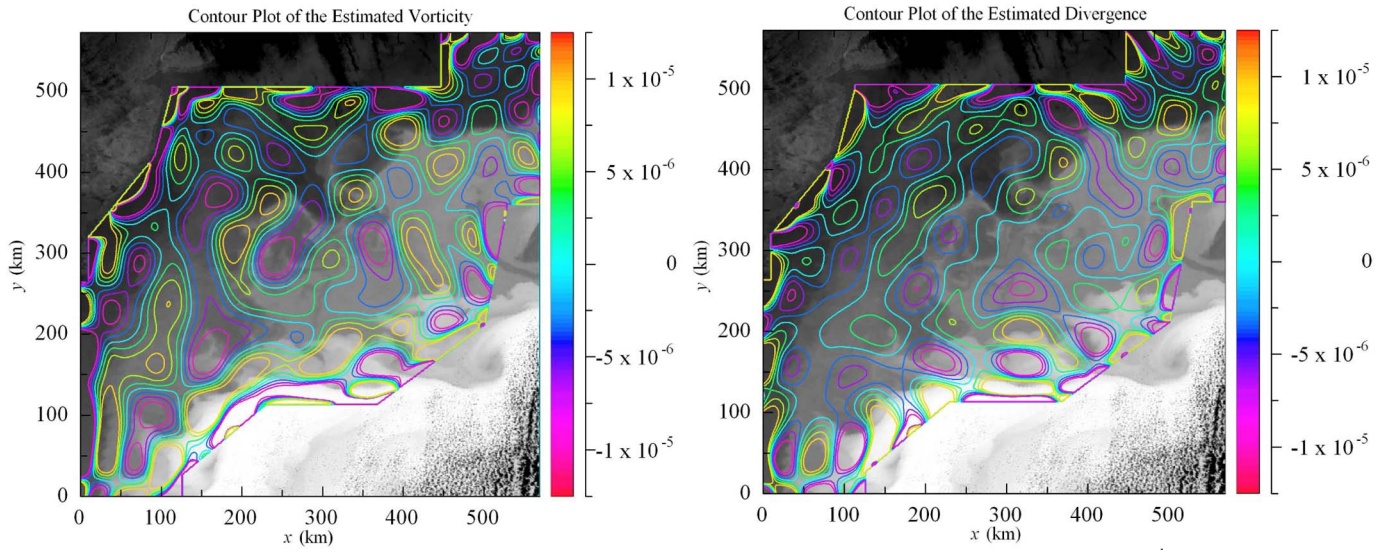

Fig. 6. Contour plots of (left) vorticity and (right) divergence are calculated from the velocity fields that are estimated by the third-order GOS technique with AVHRR image sequence on February 28, 2004 at time from 19:02 to 22:32 UT.

we see in each curve for $N \approx 10$ for the first-order GOS and $N \approx 11$ for the third-order GOS.

IV. Application to AVHRR Images

The intended application of the third-order GOS technique is to obtain an accurate estimation of the ocean surface velocity from AVHRR image sequences. We derive a velocity field from two National Oceanic Atmospheric Administration (NOAA) satellite images taken from the New York Bight, which is east of the New Jersey coast and south of Long Island, NY. These data were taken on February 28, 2004 at times $t_i =$ 19:02 and 22:32 UT [Fig. 5(a)] and on May 26, 2007 at times $t_i =$ 7:21 and 10:46 UT [Fig. 5(b)], respectively. We calculate the velocities from each of the two image pairs at contiguous times. The pixel resolutions for the images are 1.15 km in the north–south and east–west directions for the first data set and 1.008 km for the second data set in the same directions, respectively. The temporal separations between images are thus $\Delta t_i \equiv t_{i+1} - t_i = 3.500$ and 3.42 h, respectively. We examine the results over the New York Bight for the pair with the 3.42-h temporal separation and then compare the details of the flows and statistical results of velocity fields in a small region where corroborating shore-based Doppler radar coverage exists.

The northern portion of the image in Fig. 5(a) shows some atmospheric water haze contamination in the dark streaks

extending from the northern edge of the image down in a south–southeasterly direction. Their presence is also verified from the negative values delivered there by the NOAA SST algorithm. Additional cloud contamination is also clearly present in the southeastern part of the image as spotted streaks extending northward in the vicinity of the Gulf Stream (GS). The earlier image in Fig. 5(a) (at 19:02 UT and not shown here) shows a far more extensive cloud coverage over the GS. In order to apply the third-order GOS technique, we first mask the clouds and land, which is consistent with the strategy discussed in Section II-D. The resulting masked image has the form of Fig. 1, with right-angle cutouts around the edge where we have discarded any region containing clouds (in the north and south) or land (toward the west).

The major advantage of the new GOS algorithms is that it yields continuous spatial derivatives of the velocity field, which allows us to extract computed quantities such as the vorticity and divergence without any additional processing. In contrast, the first-order GOS can only provide a continuous velocity field (first order only), but the derivatives of the field with respect to x and y are not continuous. Therefore, we have to process the estimated velocity field by smoothing algorithms before computing the vorticity and divergence with the previous version of GOS. However, the degree of continuity of the velocity field estimated by the current version of GOS is easily controlled by this algorithm [we can control the order of B-spline functions by selecting the number of n's defined in (2)]. Therefore, the vorticity and divergence can be calculated directly from the estimated velocity field.

In Fig. 6, we show the contour plots of the calculated vorticity $(\xi = \nu_x - u_y)$ and divergence $(\zeta = u_x + \nu_y)$, computed from the AVHRR image sequence from 19:02 to 22:32, with u and ν inferred from the third-order GOS. The contour increment is 5×10^{-6}/s, and the interval represented is $-1.5 \times 10^{-5}\text{/s} < \xi < +1.5 \times 10^{-5}$/s, which are on the order of the Coriolis frequency (and are typical vorticity magnitudes for this region).

There are several regions shown in Fig. 6(a), for which there is a strong visual correspondence between the computed vorticity distributions and the shape of the SST distribution. In each of these locations, we see that the vorticity distribution is consistent with the sense of tracer advection of the SST field. First, there is a streamer of warm GS water attached to the GS and being advected anticyclonically around the ring (the center at position $x \approx 400$ and $y \approx 320$ with a diameter of about 100 km); it extends from the three o'clock position to the nine o'clock position. This bulk clockwise circulation is evident in all of the velocity fields retrieved from the GOS method. Fig. 6(a) shows the vorticity contours and a representative anticyclonic swirl distribution [14], [15]. The details of the velocity distribution are not critical for this illustration, and we have sketched this example (and those below) only to capture the typical properties of the expected flow field. The velocity at the center of the ring increases from zero to an anticyclonic maximum at a finite radius and then decreases at larger radii. The consequences of this typical velocity distribution are that the vorticity is negative near the ring center and positive away from it. Indeed, we see that the contours in Fig. 6(a) are blue $(\xi < 0)$ for small radii and red $(\xi > 0)$ in an annulus surrounding the negative-vorticity core. The northern portion of the ring appears to possess no vorticity, only because of the absence of trackable features there. The negative-vorticity core is not circular, which may suggest the presence of azimuthal perturbations from the assumed axisymmetric shape. Second, Fig. 6(a) shows a retrograde filament of warmer water being advected from the GS. As in Fig. 6(a) (the center of this region at position $x \approx 170$ and $y \approx 350$ with a diameter of about 100 km), we show a superposition of the SST, surface vorticity, and a nominal profile of a velocity distribution that is consistent with the observed SST deformation. We see that the northern flank of both the SST and vorticity distribution is consistent with the assumption of a rudimentary jet structure. Specifically, we note that $\xi < 0$ (purple or blue color contour) at this location. Conversely, the southern flank of the jet associated with the filament exhibits a region of red vorticity isopleths, corresponding to $\xi > 0$ there (red or yellow color contour). The vorticity, SST deformation pattern, and assumed velocity profile are thus all mutually consistent with that of an energetic jet advecting fluid from the GS. Finally, the portion of the ocean that shows the region (the center at position $x \approx 200$ and $y \approx 420$) in Fig. 6(b) is unique among the three areas shown in Fig. 6(a). This region is centered over the site, where the velocity field is diverging [in Fig. 6(b)]. The associated vorticity is compatible with this surface velocity structure. In particular, cyclonic $(\xi > 0)$ contours lie to the south of the anticyclonic $(\xi < 0)$ ones.

The GOS vectors have been superimposed on the AVHRR image from 7:21 to 10:46 UT on May 26, 2007, as shown in Fig. 5(b) and Fig. 7(b) and (c). While the evidence of organized flows is clearly evident, an excellent opportunity exists for a detailed comparison between the first- and third-order GOS velocity fields and a "ground-truth" realization of the same velocity field obtained from the Rutgers University Coastal Radar (CODAR).

This CODAR array has a resolution of 6 km and velocity magnitude and direction accuracies of ± 0.04 cm/s and $\pm 1^\circ$, respectively [12]. We plot the CODAR and corresponding first- and third-order GOS velocity fields for the time interval from 7:21 to 10:46 in Fig. 7. The radar field at the midpoint of the image time has been derived from interpolating the Rutgers hourly records [11]. The CODAR and first- and third-order GOS flows in Fig. 7 agree qualitatively, although the details of each may differ in specific locations. In general, there is a flow from the north toward the south for this time interval.

The aforementioned discussion is merely qualitative, but a quantitative comparison can be made between the first- and third-order GOS predictions and CODAR velocities by comparing their magnitudes and directions. To do this, we still use the angular and magnitude errors defined by (10) and (11), respectively, to evaluate the errors of these estimations. The results of calculating the angular and magnitude errors are shown in Fig. 8 for both the first- and third-order GOS velocity fields for the time interval from 7:21 to 10:46. Comparing the angular and magnitude errors by the first- and third-order

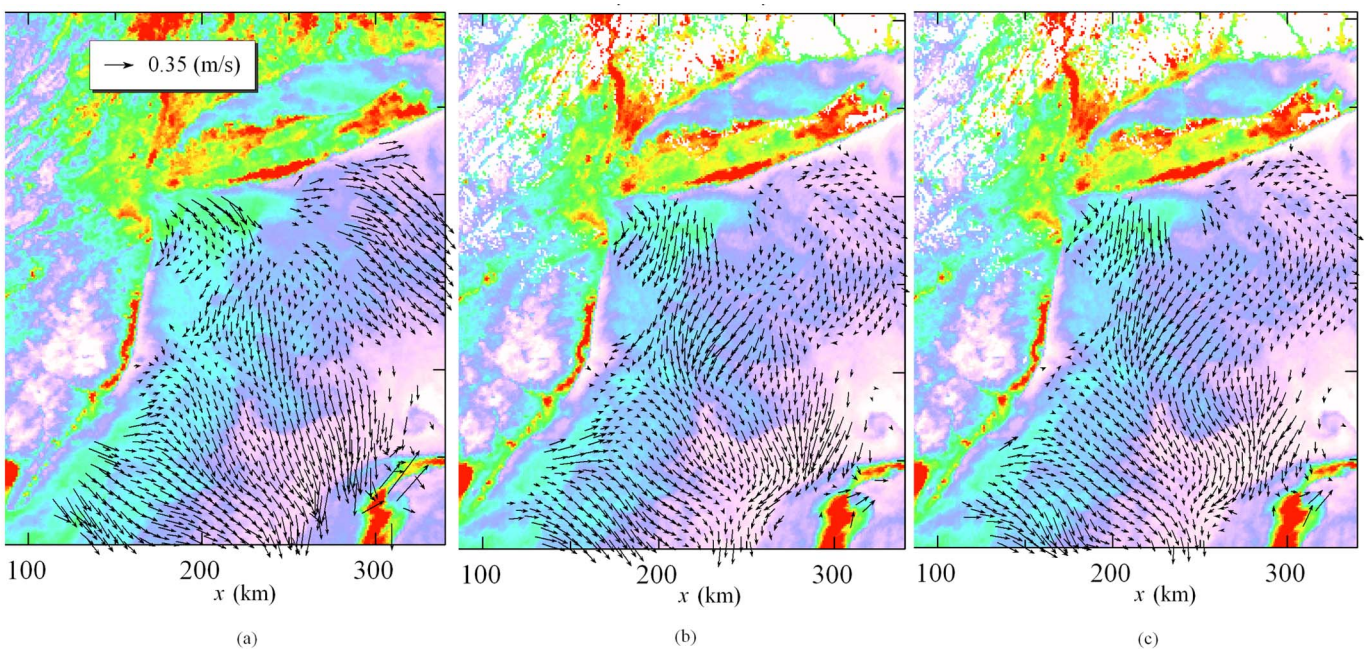

Fig. 7. Vector field derived from the AVHRR image sequence (false-color representations) from 7:21 to 10:46 UT on May 26, 2007 within an unmasked region. (a) Average CODAR velocity field (background image at 7:21 UT). (b) and (c) Estimated velocity fields by the first- and third-order GOSs (background images at 10:46 UT).

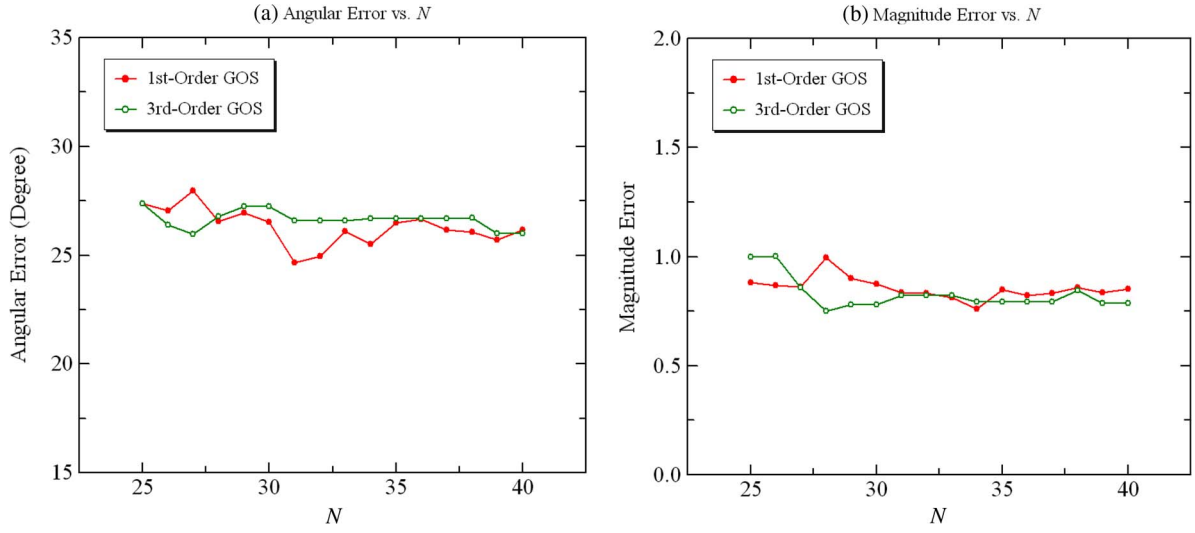

Fig. 8. Plots of error measurement generated by the first- and third-order GOSs with AVHRR data from 7:21 to 10:46 UT on May 26, 2007. (a) Mean values of angular error defined by (10) versus N (a number of pixels between two control points). (b) Mean values of magnitude error defined by (11) versus N.

GOSs, we can see that both GOS values are quite close in Fig. 8 within the whole range for N.

V. Conclusion

A higher order GOS inverse technique to obtain near-surface velocity from sequential infrared images has been presented. Two-dimensional B-spline functions over the whole unmasked image scenes are used to convert the inverse problem from a locally underdetermined system of equations to an overdetermined one. At those locations where land or clouds occupy a portion of B-spline functions, the array is discarded (Fig. 1), and a "mask" is generated.

The resulting third-order GOS velocity fields have been compared with those from the numerical model and from the first-order GOS technique (see [10]). The calculation of the angular and magnitude error difference between the first- and third-order GOS results and the model or CODAR velocities indicates that the GOS/model or GOS/CODAR errors are quite close (Figs. 4 and 8), but the new GOS algorithms allow us to generate high-order continuity velocity fields and deal with the shoreline or contaminated regions easily.

This paper has aimed at providing an accurate technique to estimate sea-surface velocities from satellite SST fields. In addition, the problem of solving the heat equations becomes solving linear system equations by the GOS algorithms. The

velocity field expanded by surface B-spline functions that allow us to select the order of continuity for different applications is globally smoothed [Fig. 3(c) and (f)]. Adjusting the number of control points in the B-spline functions, we can restrain the noise for real image data efficiently (see [10] for the first-order GOS) and obtain a scalable spatial resolution of the velocity field. The field estimated by higher order GOS can be used to extract the computed quantities such as the vorticity and divergence without additional processing, and the handling of complicated coastal land boundaries and cloud contamination becomes a much easier process.

These numerical results have provided an important test of the reliability of the first- and third-order GOSs. In order to gain a further understanding of the usefulness of the GOS method and to see if further insight could be obtained into the underlying dynamics, I have provided the examples of the surface vorticity and divergence calculations based on the velocity field estimated by the third-order GOS with realistic AVHRR image sequence in the New York Bight. I have found that at least three interesting examples of vorticity structures emerge: a warm core ring, a GS filament, and a divergent region. This last scenario is located in the northern part of the region. In all these cases, the computed vorticity distributions are consistent with the inferred velocity patterns required for the observed kinematic distortions of the tracer.

ACKNOWLEDGMENT

The author would like to thank Prof. J. Kohut (Rutgers University) for supplying the CODAR velocity field used in this paper.

REFERENCES

[1] K. A. Kelly, "An inverse model for near-surface velocity from infrared images," *J. Phys. Oceanogr.*, vol. 19, no. 12, pp. 1845–1864, Dec. 1989.

[2] K. A. Kelly and P. T. Strub, "Comparison of velocity estimates from Advanced Very High-Resolution," *J. Geophys. Res.*, vol. 97, pp. 9653–9668, 1992.

[3] A. Ostrovskii and L. Piterbarg, "Inversion for heat anomaly transport from sea-surface temperature time-series in the northwest Pacific," *J. Geophys. Res.*, vol. 100, no. C3, pp. 4845–4865, 1995.

[4] A. G. Ostrovskii and L. I. Piterbarg, "Inversion of upper ocean time series for entrainment, advection, and diffusivity," *J. Phys. Oceanogr.*, vol. 30, no. 1, pp. 201–214, Jan. 2000.

[5] X. Vigan, C. Provost, R. Bleck, and P. Courtier, "Sea surface velocities from sea surface temperature image sequences 1. Method and validation using primitive equation model output," *J. Geophys. Res.*, vol. 105, no. C8, pp. 19 499–19 514, 2000.

[6] X. Vigan, C. Provost, R. Bleck, and P. Courtier, "Sea surface velocities from sea surface temperature image sequences 2. Application to the Brazil–Malvinas confluence area," *J. Geophys. Res.*, vol. 105, no. C8, pp. 19 515–19 534, 2000.

[7] P. O. Zavialov, R. D. Ghisolfi, and C. A. E. Garcia, "An inverse model for seasonal circulation over the southern Brazilian shelf: Near-surface velocity from the heat budget," *J. Phys. Oceanogr.*, vol. 28, no. 4, pp. 545–562, Apr. 1998.

[8] S. Côté and A. R. L. Tatnall, "The use of the Hopfield neural network to measure sea-surface velocities from satellite images," *IEEE Geosci. Remote Sens. Lett.*, vol. 4, no. 4, pp. 624–628, Oct. 2007.

[9] J. Marcello, F. Eugenio, F. Marqués, A. Hernández-Guerra, and A. Gasull, "Motion estimation techniques to automatically track oceanographic thermal structures in multisensor image sequences," *IEEE Trans. Geosci. Remote Sens.*, vol. 46, no. 9, pp. 2743–2762, Sep. 2008.

[10] W. Chen, R. P. Mied, and C. Y. Shen, "Near-surface ocean velocity from infrared images: Global optimal solution to an inverse model," *J. Geophys. Res.*, vol. 113, no. C10, p. C10 003, 2008.

[11] S. R. Chubb, R. P. Mied, C. Y. Shen, W. Chen, T. E. Evans, and J. Kohut, "Ocean surface currents from AVHRR imagery: Comparison with land-based HF radar measurements," *IEEE Trans. Geosci. Remote Sens.*, vol. 46, no. 11, pp. 3647–3660, Nov. 2008.

[12] J. T. Kohut, S. M. Glenn, and R. J. Chant, "Seasonal current variability on the New Jersey inner shelf," *J. Geophys. Res.—Oceans*, vol. 109, no. C7, p. C07 S07, 2004.

[13] A. Watt and M. Watt, *Advanced Animation and Rendering Techniques—Theory and Practice*. Reading, MA: Addison-Wesley, 1992, pp. 89–110.

[14] G. R. Flierl and R. P. Mied, "Frictionally induced circulations and spin down of a warm-core ring," *J. Geophys. Res.—Oceans*, vol. 90, no. C5, pp. 8917–8927, 1985.

[15] T. A. Joyce and M. A. Kennelly, "Upper-ocean velocity structure of Gulf Stream warm-core ring 82B," *J. Geophys. Res.*, vol. 90, no. C5, pp. 8839–8844, 1985.

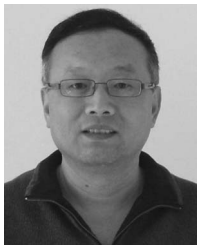

Wei Chen received the B.S. degree in physics from Nankai University, Tianjin, China, in 1982 and the Ph.D. degree in physics from Brigham Young University, Provo, UT, in 1991.

He held a postdoctoral position at the National Institute of Standard and Technology, Gaithersburg, MD. Since 1999, he has been a Research Physicist with the Remote Sensing Division, Naval Research Laboratory, Washington, DC. He designed, developed, and implemented independently several software packages which include PlotInfinity and MathInfinity (Computer Algebra System). His areas of research include solid-state physics, computer science, image processing, and remote-sensing applications in oceanography.